Improving LiFe0.4Mn0.6PO4 Nanoplates Performances by a Dual Modification Strategy toward Practical Application of Li-Ion Batteries

Helei Wei , Mingfeng Tan , Qi Li , Zhipeng Yu , Bo Lin *

Posted Date: 16 May 2024

doi: 10.20944/preprints202405.1101.v1

Keywords: fluorine-doped carbon; graphene; lithium manganese phosphate; uniform coating; li-ion battery

Article

Improving $LiFe_{0.4}Mn_{0.6}PO_4$ Nanoplates Performances by a Dual Modification Strategy toward Practical Application of Li-ion Batteries

Helei Wei [1], Mingfeng Tan [1], Qi Li [1], Zhipeng Yu [2] and Bo Lin [1,*]

[1] Global R&D Center, Guangxi Liugong Machinery Co., Ltd., Liuzhou, Guangxi 545007, China; weihelei@liugong.com (H.W.); tanmingfeng@liugong.com (M.T); liqi@liugong.com (Q.L)
[2] International Iberian Nanotechnology Laboratory (INL) Avenida Mestre Jose Veiga, 4715-330 Braga, Portugal; zhipeng.yu@inl.int
* Correspondence: linbo@liugong.com

Abstract: A novel composite consisting of fluorine-doped carbon and graphene double-coated $LiMn_{0.6}Fe_{0.4}PO_4$ (LMFP) nanorods, synthesized via a facile low temperature solvothermal method that employs a hybrid glucose and polyvinylidene fluoride as carbon and fluorine sources. As revealed by physicochemical characterization, F-doped carbon coating and graphene form a 'point-to-surface' conductive network, facilitating rapid electron transport and mitigating electrochemical polarization. Furthermore, the uniform thickness of the F-doped carbon coating alters the growth of nanoparticles and prevents direct contact between the material and the electrolyte, thereby enhancing structural stability. Strong electronegative F^- is beneficial to inhibit the structural changes of LMFP caused by Li-insertion/extraction during charge/discharge, which effectively reduces the Jahn-Teller effect, and inhibits Mn dissolution. The distinctive architecture of LMFP/C-F/G cathode material exhibits excellent electrochemical properties, exhibiting an initial discharge capacity of 163.1 mAh g^{-1} at 0.1 C and a constant Coulombic efficiency of 99.7% over 100 cycles. Notably, LMFP/C-F/G cathode material achieves an impressive energy density of 607.6 Wh kg^{-1}, surpassing that of commercial counterparts. Moreover, it delivers a reversible capacity of 90.3 mAh g^{-1} at a high current rate of 5 C. The high capacity capability and energy density of the prepared materials give them great potential for use in next-generation lithium-ion batteries.

Keywords: fluorine-doped carbon; graphene; lithium manganese phosphate; uniform coating; li-ion battery

1. Introduction

Enhancement of lithium-ion battery performance relies significantly on the positive electrode material [1,2]. Therefore, the study of positive electrode materials is crucial in both scientific and industrial fields. Among them, the olivine-type structure of polyanionic phosphate positive electrode materials is considered to have immense potential for development owing to its excellent performance [3]. In 1997, Goodenough et al.[4] discovered that lithium iron phosphate (LFP) material possesses lithium-insertion/extraction properties, garnering significant attention as a polyanionic LiMPO4 (M=Fe, Mn, Ni, Co, etc.) cathode material. Notably, with the tetrahedral PO_4^{3-} polyanion structure, the P–O bond exhibits strong covalency [5]. This not only prevents the release of oxygen release but also stabilises the ionic covalency of the M(3d)–O(2p) bond through inducing effects, thereby enhancing the stability of $LiMPO_4$ [6]. Among developed $LiMPO_4$ materials, LFP has undergone rapid industrialization owing to its advantages such as long cycle life, high safety, and low cost [7,8]. However, LFP material still encounters limitations: First, it exhibits lower electronic and ionic conductivity at room temperature than lithium cobalt and lithium manganate [9]; Second, the energy density of the LFP cathode material (578 Wh kg^{-1}) nears its limit owing to its low operating

 doi:10.20944/preprints202405.1101.v1

voltage (3.4 V vs. Li^+/Li) and theoretical capacity (170 mAh g^{-1}), which makes it difficult to meet the increasing demands for high energy and long-term endurance in electric vehicles [10]. Consequently, improving its electron/ion conductivity and energy density has become paramount.

In recent years, a $LiMn_xFe_{1-x}PO_4$ ($0 \le x \le 1$) material with high energy density has been considered an upgraded version of LFP [11,12]. Studies have shown that constructing a structure with x = 0.6 is the most suitable scheme for achieving the optimal rate capability and energy density [13,14]. However, the practical application of LMFP encounters challenges, such as weak electron transport and Li^+ diffusion ability, and structural instability due to Mn^{3+} dissolution [15,16]. To address these issues, research on LMFP has focused on modifying both external surfaces and internal structures. External surface modification typically involves applying a barrier layer onto the olivine structure to enhance the electronic/ionic conductivity of the material, while reducing the contact area between the main material and electrolyte to effectively inhibit electrolyte decomposition and improve cycling stability [17,18]. Additionally, this process can partially suppress the Jahn-Teller effect by applying additional pressure on the internal crystals through the surface coating, thereby reducing the probability of microcrack formation. Internal structure modification focuses on controlling the crystal size [19,20], regulating crystal structure order [21,22], and achieving a specific distribution of Mn/Fe atoms [23,24] to accelerate electrochemical activity and enhance battery performance. Therefore, deliberately controlling the crystal growth conditions to produce high-quality $LiMn_{0.6}Fe_{0.4}PO_4$ cathode materials is crucial for promoting its commercial application.

Compared to the solid-phase method, hydrothermal synthesis represents is a feasible strategy for effectively controlling crystal growth at the atomic level [8]. Nucleation and crystal growth can be controlled by adjusting the temperature, reaction time, and heating rate [25]. Furthermore, different solvents provide options for controlling the crystallinity and nanomorphology [26]. Many hydrothermal synthesis methods currently achieve excellent performance materials at high temperatures (approximately 180 °C), which are not conducive to industrial production and management. Therefore, developing a low-temperature synthesis method for LMFP industrialization is important.

In this study, we employed an environmentally friendly and efficient low-temperature solvothermal reaction to synthesize the nanorod-like $LiMn_{0.6}Fe_{0.4}PO_4$ (LMFP) cathode material with enhanced electrochemical reaction kinetics. We investigated the effects of the crystallinity, orientation, morphology, particle size, and electrochemical properties of LMFP. Due to the low electronic conductivity of the synthesized LMFP sample, we used doping and carbon coating modifications to enhance its electrochemical performance [27]. Previous studies have demonstrated that doping with the highly electronegative F element can effectively enhance lithium-ion adsorption and promote electrode reactions [28]. In addition, the carbon-coated and graphene-constructed 'point-to-surface' combined network structure provides rapid channels for electron and ion transport [29]. Consequently, LMFP/C-F/G materials exhibit high capacity, excellent rate performance, and high energy density, providing a strong foundation for the commercial application of LMFP.

2. Results and Discussion

2.1. Material Synthesis and Characterization

Synthesis of $LiFe_{0.4}Mn_{0.6}PO_4$: Typically, the cathode materials were prepared by the solvothermal method. $LiOH·H_2O$, $MnSO_4·H_2O$, $FeSO_4·7H_2O$, H_3PO_4 (mass fraction 85%) were used as raw materials, L(+)-ascorbic acid was used as an antioxidant. The solvent was a mixture of DMF and water, the solvent ratio of V_{DMF}/V_{H2O} =1. Firstly, add a certain amount of $LiOH·H_2O$ and H_3PO_4 in the solvent, and use the ultrasonic machine to fully dissolve the raw material and form a white suspended substance Li_3PO_4. Then a certain amount of manganese source, iron source and L(+)-ascorbic acid are added to the solvent, and the raw materials are fully dissolved by ultrasound. The above two solutions were fully mixed and transferred to a 100 mL Teflon-lined autoclave for solvent-thermal reaction in a blast oven. The above two solutions are fully mixed and transferred to a blast drying oven for solvent-thermal reaction. The ash black precursor powders $LiFe_{0.4}Mn_{0.6}PO_4$ was obtained after centrifugation and drying, denoted as LMFP.

 doi:10.20944/preprints202405.1101.v1

Synthesis of LMFP/C: For LMFP/C, the mass of glucose added accounts for 10 wt.% of the precursor LMFP, and is fully mixed and ground. Then, the dried product was heated in inert atmosphere at 600 °C for 8 h to obtain LMFP/C.

Synthesis of LMFP/C/G: For LMFP/C-G, the synthesis steps were the same as for LMFP/C, the only difference is that only graphene is added, named as LMFP/C/G.

Synthesis of LMFP/C-F/G: For LMFP/C-F/G, the synthesis steps were the same as those for LMFP/C-F/G, the only difference was that only graphene was added PVDF is added as the F source, named as LMFP/C-F/G.

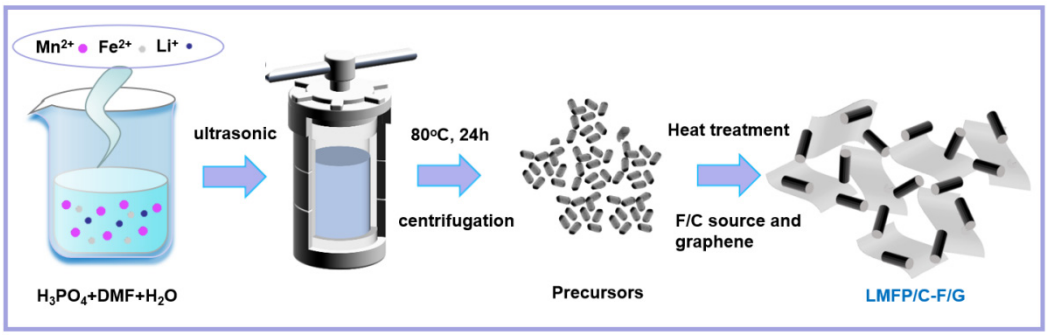

Scheme 1. Schematic illustration of the synthesis process.

Some experiments have indicated that the rate performance enhancement of samples prepared by directly coating graphene on the surface of cathode materials using the hydrothermal method is unsatisfactory, potentially due to stacking or destruction of the graphene material structure [30]. Moreover, complete coating results in a decrease in ion transport efficiency, which is hypothesized to be caused by lithium ions being unable to pass through the six-membered ring structure of graphene [31,32]. Given the above, we have developed a 'point-to-surface' conductive network where graphene exists in a partially coated state. This design facilitates rapid lithium ion transport and enhances conductivity (as illustrated in Scheme 1). The mechanism involves incorporating graphene material between the LMFPs in a layered structure, similar to building a 'bridge' for electron conduction.

X-ray diffraction (XRD) was utilized to identify the crystal structure of the prepared cathode materials in this study (Figure 2a). As depicted in Figure 1a, the diffraction peaks at 16.9°, 20.7°, 25.4°, 29.5°, 35.3° and 52.2° correspond to the (020), (011), (111), (200), (131) and (321) planes of the standard diffraction peak of orthorhombic Pmnb's (LMFP: PDF#11-0456) for both LMFP/C, LMFP/C/G and LMFP/C-F/G, respectively, indicating that all carbon-coated and doped materials were pure phase. Furthermore, the sharp diffraction peaks indicated a high crystallinity intensity for the three LMFP materials, with the highest diffraction peak located in the (131) crystal plane. There is no additional diffraction peak, indicating that the lattice structure of LMFP/C remains intact despite the slight F-doping and trace graphene introduction [27]. Notably, no diffraction peaks of carbon were found either, indicating the possible formation of amorphous carbon, which was subsequently confirmed by TEM characterization. Moreover, no graphene (002) diffraction peak was found, because the low content of graphene and the strong LFMP (111) diffraction peak occurring at the same 2θ angle [33].

 doi:10.20944/preprints202405.1101.v1

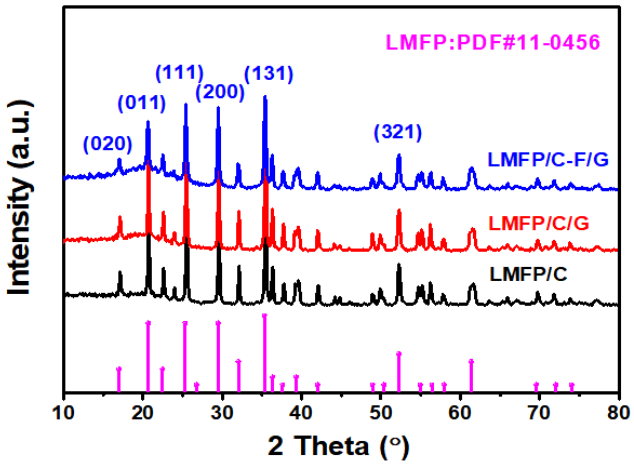

Figure 1. XRD spectra of the LMFP/C, LMFP/C/G and LMFP/C-F/G.

Transmission electron microscopy (TEM) was used to investigate the effects of F-doping and coating strategies on the microstructure and morphology of LMFP/C-F/G materials. As shown in Figure 2a,b, the LMFP/C-F/G exhibit a nanorod morphology with a length of 50-400 nm and width of 40-80 nm, which is consistent with the observations from scanning electron microscopy (SEM) images (Figures S1). In addition, it is evident that the carbon coating material and graphene constitute a "point-to-surface" conductive network, which significantly enhances the electronic conductivity of the LMFP material. The excellent electrochemical performance of the LMFP/C-F/G could be attributed to the successfully synthesis of the hierarchical and bridging structure that ensures a uniform coating of the amorphous carbon closely linked with high electrical conductivity provided by graphene.

To determine the large exposed surface, internal structure and lattice growth mechanisms of the LMFP/C-F/G nanorods, the material was deeply characterized using high-resolution TEM (HRTEM). The underlined part is the amorphous carbon with a thickness of approximately 4.0 nm, formed by the carbonation of the added glucose and PVDF (Figure 2c,d), which was observed on the surface of the particles. This uniform coating of amorphous carbon plays a crucial role in inhibiting further crystal growth during sintering and enhancing the material's electronic conductivity. On the one hand, these amorphous carbons improve the conductivity of the LMFP material, on the other hand, they prevent the increase of the size of the LMFP nanoparticles and inhibit the dissolution of Mn. Furthermore, Figure 2h shows well-resolved lattice fringes with a d-spacing of 0.349 nm, which correspond to the (111) lattice plane of LMFP.

Elemental mapping results are shown in Figure 2e–i. It is seen that the C, O, Mn, Fe, F, and P elements are uniformly distributed over the LMFP nanoparticle. This observation signifies the successful doping of element F into the material, thereby imparting excellent electronic conductivity to it.

 doi:10.20944/preprints202405.1101.v1

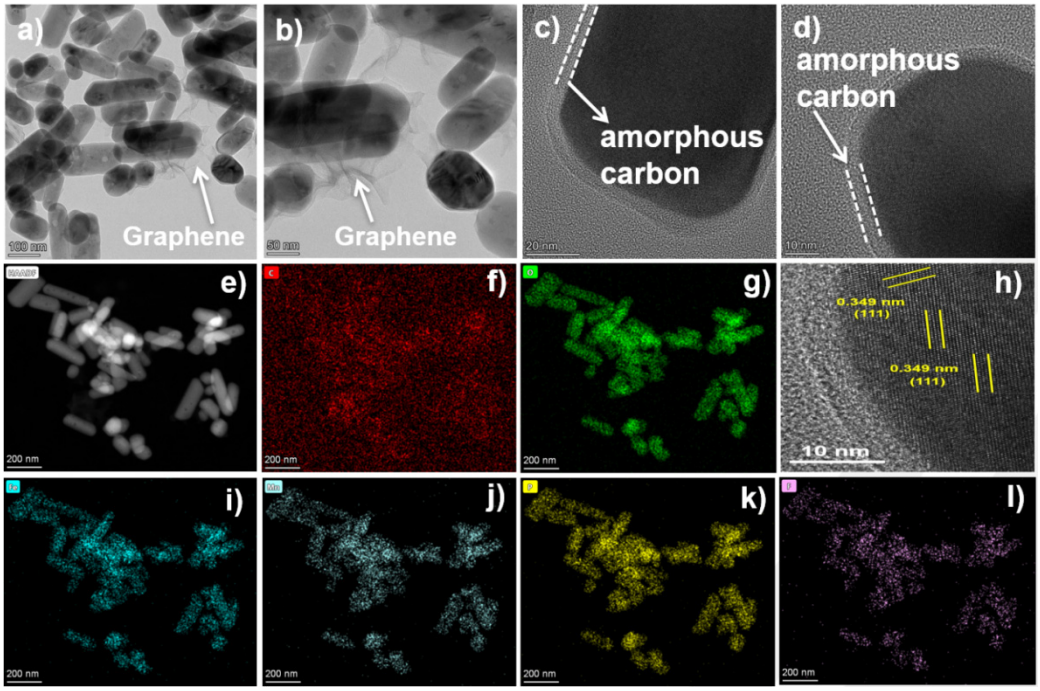

Figure 2. a-b) TEM image and c-d) HRTEM image of LMFP/C-F/G, e-i) corresponding elemental mapping images of LMFP/C-F/G.

The surface elemental composition and chemical state are investigated by X-ray photoelectron spectroscopy (XPS, Figures 3, S2 and S3) [34]. All of the binding energy of the spectra was calibrated by using the reference peak at 284.6 eV for C 1s. The survey spectrum of LMFP/C-F/G exhibited the signals of Li 1s, C 1s, O 1s, F 1s, Fe 2p, Mn 2p and P 2p elements (Figure 3). The content of the elements is summarized in Table 1 and it can be found that the molar ratio of Fe/Mn is approximately 4/6, which corresponds to the feeding ratio.

Table 1. Elemental composition (at %) measured by XPS.

Sample	C	O	F	Li	Fe	Mn	P	Fe:Mn
LMFP/C	29.55	25.83	--	33.92	1.53	2.42	6.75	4:6
LMFP/C/G	49.25	22.00	--	50.88	1.02	1.60	4.19	4:6
LMFP/C-F/G	39.38	22.40	0.28	29.33	1.28	1.94	5.38	4:6

High-resolution XPS spectra revealed that the Fe 2p spectrum (Figure 3b) is split into two peaks at about 710.9 and 724.3 eV, which correspond to Fe 2p3/2 and Fe 2p1/2, respectively [35]. The results confirm that the oxidation state of Fe is 2+. Additionally, two peaks at energies of around 712.8 and 727.5 eV are identified as satellite features related to Fe^{2+}[36].

Preprints.org (www.preprints.org) | NOT PEER-REVIEWED | Posted: 16 May 2024 doi:10.20944/preprints202405.1101.v1

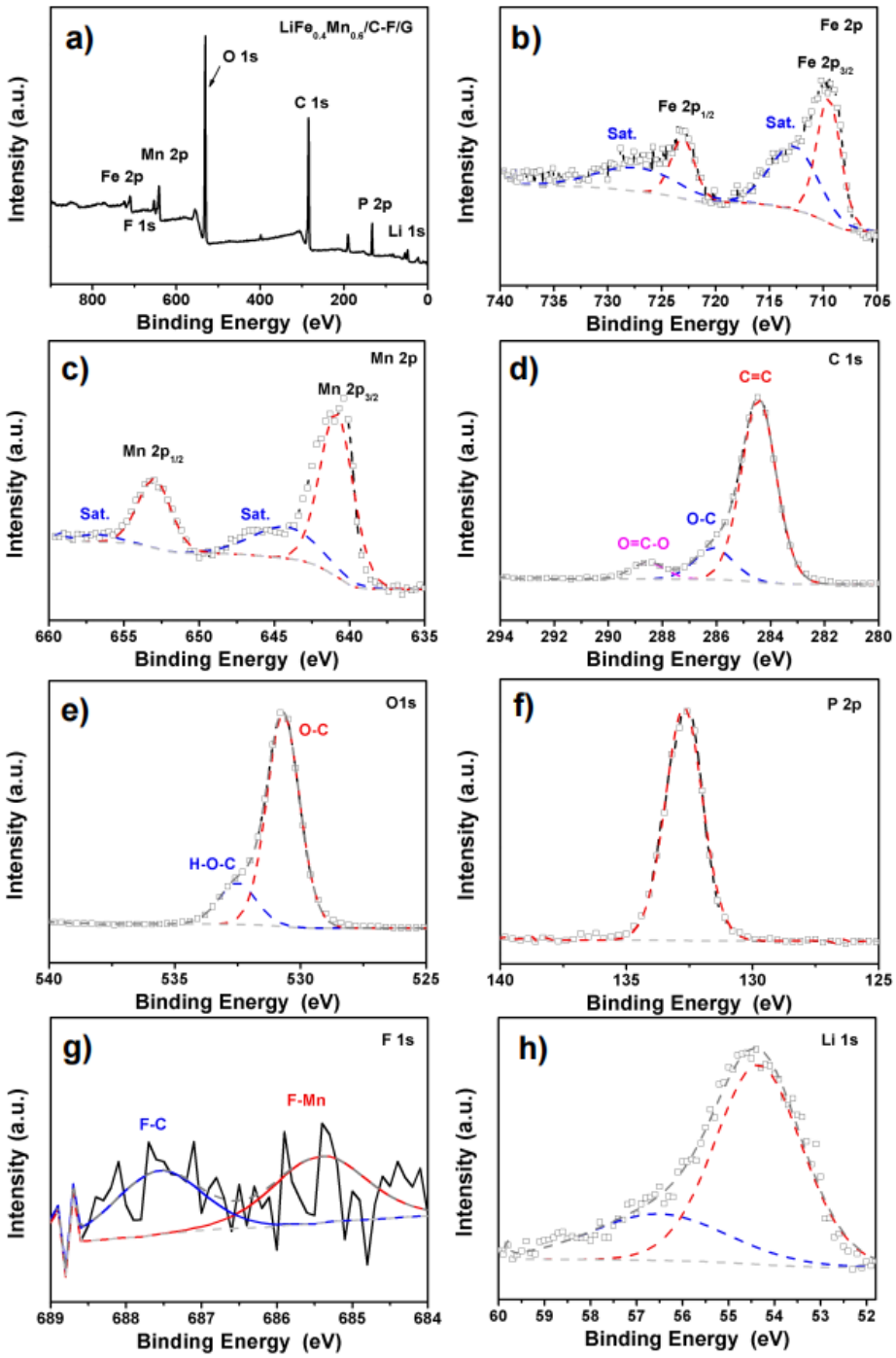

Figure 3. a) XPS survey spectra of LMFP/C-F/G and the high-resolution spectrum of b) Fe 2p; c) Mn 2p; d) C 1s; e) O 1s; f) P 2p; g) F 1s; h) Li 1s.

As shown in Figure 3c, the Mn 2p spectrum is split into two peaks at approximately 640.9 and 653.0 eV, which can be ascribed to Mn 2p3/2 and Mn 2p1/2, respectively. The results confirm that the oxidation state of Mn is 2+ [37]. The C 1s high-resolution XPS spectrum can be fitted into three peaks (Figure 3d). The dominant binding energy located at 284.6 eV is ascribed to the C-C bond. The peak located at about 286.1 eV corresponds to the C-O bond configuration [38]. In addition, the peak at approximately 288.5 eV is attributed to O=C-O or C-F chemical bond [39]. The peaks located at about 132.6 and 530.6 eV are ascribed to P 2p and O 1s, which belong to tetrahedral PO_4^{3-} groups (Figure 3e,f). As shown in Figure 3g, two weak peaks located at about 685.4 and 687.5 eV belong to F-Mn and F-C chemical bond, respectively [40]. This result suggests that F atoms are doped in the carbon

 doi:10.20944/preprints202405.1101.v1

coating, it not only acts as a lithium reservoir to stabilize the electrode, but also as a composite current collector to manage nucleation/growth of lithium [41], which is beneficial to reducing the charge transfer resistance and inhibiting the Jahn-Teller effect. The binding energy is divided into two fitted peaks in the 52-60 eV region, corresponding to the oxidation state of Li (Figure 3h). These results provide compelling evidence for the successful synthesis of LMFP/C-F/G cathode material.

2.2. Electrochemical Performance and Analysis

Cyclic voltammogram (CV) and electrochemical impedance spectroscopy (EIS) were used to investigate the effect of F-doping and carbon coating on the electrochemical properties, electronic conductivity and electrode kinetic parameters of the LMFP (Figure 4). Figure 4a illustrates the CV diagram of three LMFP materials prepared under 1.0 mV s−1. The cyclic voltammetry curves have two pairs of distinct peaks near 3.5 V and 4.1 V, which correspond to the redox peaks of Fe2+/Fe3+ and Mn2+/Mn3+, respectively. The trend of peak width of the three materials is the same, but the peak and peak sharpness are different. As shown in Table 2, the voltage difference between oxidizing and reducing peaks of the LMFP/C-F/G is the smallest of all the samples (for manganese site, LMFP/C-F/G (0.36 V) < LMFP/C/G (0.40 V) < LMFP/C (0.56 V), for manganese site, LMFP/C-F/G (0.25 V) < LMFP/C/G (0.27 V) < LMFP/C (0.45 V), respectively), which is probably because the introduction of trace amounts of F and graphene promotes the transport of Li+ and reduces polarization of the cathode. In addition, the peak shape of the LMFP/C-F/G electrode is sharper, indicating that it has faster reaction kinetics, which also matches its excellent Li+ diffusion rate and optimal performance.

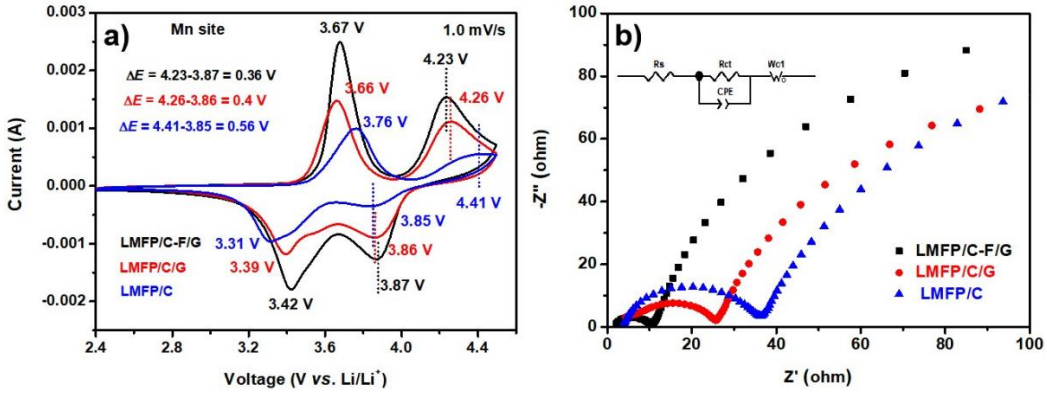

Figure 4. a) CV curves at a scan rate of 1.0 mV s^{-1} and b) electrochemical impedance spectroscopy patterns of LMFP/C, LMFP/C-F and LMFP/C-F/G.

Table 2. Redox potential difference in CV curves for three samples.

Sample	Fe^{3+}	Fe^{2+}	Mn^{3+}	Mn^{2+}	ΔE_{Fe}	ΔE_{Mn}
LMFP/C	3.76	3.31	4.41	3.85	0.45	0.56
LMFP/C/G	3.66	3.39	4.26	3.86	0.27	0.40
LMFP/C-F/G	3.67	3.42	4.23	3.87	0.25	0.36

2.3. Mechanism Analysis of the Electrocatalytic Activity Enhancement

The electrochemical kinetics of the cathode material were further investigated by performing electrochemical impedance spectroscopy (EIS) measurements after CV cycling. The Nyquist plots (Figure 4b) exhibit a compressed semicircle in high-to-medium frequency followed by an oblique line in the low-frequency. The intercept with the Z' axis in the high-frequency region is associated with the ohmic resistance (R_s), which describes the sum of the resistance between cathode material, electrolyte, and separator [42]. The following semicircle in the high and middle-frequency regions refers to the charge transfer resistance (R_{ct}), which describes the resistance of the electrochemical reaction at the electrolyte/electrode interface. The oblique line in the low-frequency reflects the

 doi:10.20944/preprints202405.1101.v1

Warburg impedance, which relates to Li-ion diffusion in the cathode material particles [43]. By comparing the diameters of semicircles, it can be inferred that LMFP/C-F/G cathode exhibits lower charge transfer resistance compared to LMFP/C/G and LMFP/C (Figure 4b), suggesting the improved charge transfer kinetics and ionic conductivity induced by the co-modification of F-dopping and carbon graphene network.

To further investigate the electrochemical kinetics of the cathode material, we tested CV at different sweep speeds and performed a fitting analysis. Figure 5 shows the CV curves of cathodes LMFP/C-F/G, LMFP/C/G and LMFP/C at different scanning rates and the corresponding linear fitting between I_p and $v^{1/2}$. It can be noticed that the peak current increases gradually with the increase of scanning rate. Compared to other cathodes, the cathode LMFP/C-F/G has a larger peak current and integration area, and better symmetry of the redox curve, which indirectly indicates a better performance. As shown in Equation 1, the lithium-ion diffusion coefficient D_{Li+} of the cathode material was calculated from the Randles-Sevcik formula [44,45].

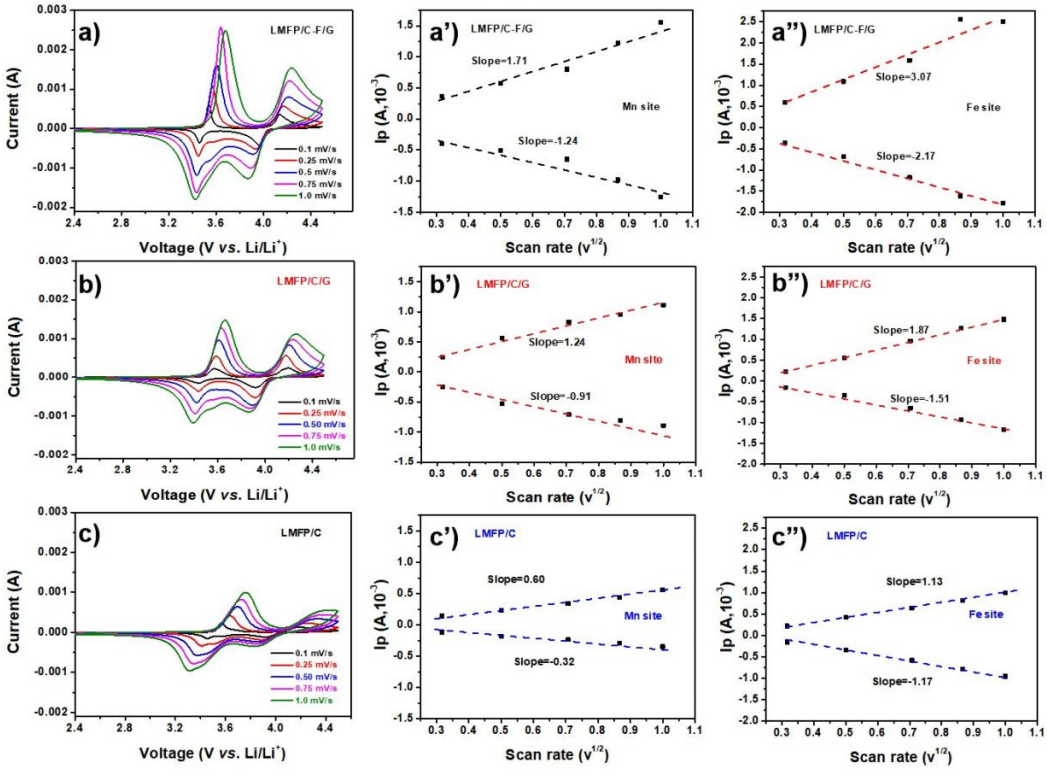

Figure 5. Cyclic voltammetry curves of cathode a) LMFP/C-F/G, b) LMFP/C/G, and c) LMFP/C at varies scanning rates. Linear fitting of I_p vs. $v^{1/2}$ for cathode LMFP/C-F/G (a′ and a′′), LMFP/C/G (b′ and b′′) and LMFP/C (c′ and c′′) at corresponding Mn and Fe redox peaks.

$$I_p = 2.69\times10^5\, n^{3/2} A D^{1/2} C v^{1/2} \quad (1)$$

where I_p is the peak current (A), n is the number of electrons transferred by the material during the electrochemical reaction, A is the specific surface area of the electrode active material (cm^2), D is the Li-ion diffusion coefficient in LMFP at 298 K ($cm^2\ s^{-1}$), C is the molar concentration of Li ions in the cathode material (0.0223 mol cm^{-3}), and v is the scan rate (V s^{-1}).

According to the formula, it can be observed that under identical conditions for other variables, the diffusion rate of lithium-ion D_{Li+} is positively correlated with the peak current intensity. Based on the slope analysis, it can be inferred that LFMP/C-F/G cathode material exhibits a significantly higher lithium ion diffusion rate compared to other materials (Figure 5). Specifically, by comparing the slope of Mn site and Fe site (Figure 5a′–a′′, b′–b′′ and c′–c′′), it is qualitatively deduced that F-doped carbon layer can accelerate Li^+ insertion/extraction into/from LMFP, i.e., the D_{Li+} of LMFP/C-F/G cathode is greater than those of LMFP/C/G and LMFP/C. Furthermore, the linear relationship implies that the

 doi:10.20944/preprints202405.1101.v1

intercalation and deintercalation behavior of Li^+ in the three materials are diffusion-controlled [11]. According to the slopes of the fitting lines in Figure 5, the Li-ion chemical diffusion coefficients of LMFP/C, LMFP/C/G and LMFP/C-F/G are calculated to be 3.48×10^{-14}, 5.81×10^{-14} and 1.20×10^{-13} cm^2 s^{-1}, respectively (Table S2). The LMFP/C-F/G sample shows the largest Li-ion diffusion rate, endowing it with the best rate performance.

Figure 6 illustrates the effects of carbon coating and F-doping on the electrochemical performance of LMFP/C-F/G at 25°C, including the first charge/discharge, rate performance, cycle performance, etc. As shown in Figure 6a, after several activations, their charge/discharge curves basically coincide, indicating that their coulomb efficiency is basically close to 100% and the material has good electrochemical stability.

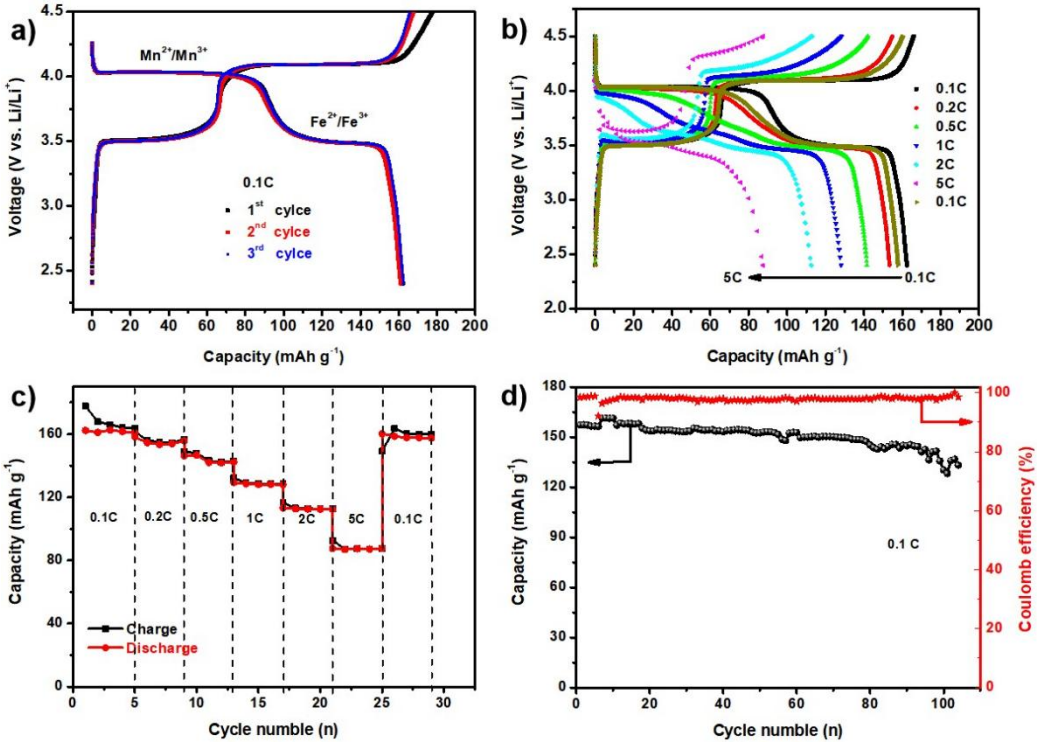

Figure 6. Electrochemical performance of LMFP/C-F/G at 25 °C: a) First three charge/discharge curves at 0.1 C; b) Rate performance at different C rates and c) Corresponding charge/discharge curves. d) Cycling performance with corresponding coulomb efficiency.

In these curves, two pairs of obvious platforms appear near 3.5 V and 4.1 V, corresponding to the oxidation-reduction potentials of Fe^{2+}/Fe^{3+} and Mn^{2+}/Mn^{3+} oxidation-reduction potentials respectively, and the ratio of platforms is approximately 6/4, which is consistent with the ratio of Mn/Fe in the material. This result is also in agreement with the results of the CV curves. It's worth noting that the first discharge capacities of LMFP/C-F/G materials were 163.1 mAh g^{-1} at the rate of 0.1 C, higher than LMFP/C/G (156.8 mAh g^{-1}, Figure S4a) and LMFP/C (146.7 mAh g^{-1}, Figure S5a, Table S1). Furthermore, benefit from the increase of its voltage and capacity, the energy density of LMFP/C-F/G (607.6 Wh kg^{-1}) is also much higher than that of LMFP/C/G (583.1 Wh kg^{-1}) and LMFP/C (550.5 Wh kg^{-1}) (Table S1). It is suggested that the construction of a 'point-to-surface' combined conductive network is beneficial for improving the performance and energy density of LMFP.

As presented in Figure 6b,c, the discharge capacity of LMFP/C-F/G sample decreased with increasing of C rates and the difference in capacity become progressively more obvious at higher rates. It's worth noting that LMFP/C-F/G delivers discharge capacities of 163.1, 155.4, 146.7, 130.1, 114.6, and 88.1 mAh g^{-1} at 0.1, 0.2, 0.5, 1, 2, and 5 C, respectively. However, LMFP/C-/G only exhibits discharge capacities of 157.8, 146.3, 135.4, 119.6, 107.5, and 81.2 mAh g^{-1} at 0.1, 0.2, 0.5, 1, 2, and 5 C, respectively (Figure S4b and Table S1). LMFP/C only exhibits discharge capacities of 146.7, 142.8,

 doi:10.20944/preprints202405.1101.v1

132.6, 118.2, 101.2, and 78.9 mAh g^{-1} at 0.1, 0.2, 0.5, 1, 2, and 5 C, respectively (Figure S5b and Table S1). Therefore, the rate capability of LMFP/C-F/G is significantly enhanced by the synergistic effect of carbon coating and F-dopping dual strategies. Figure 6d shows the cycle stability of the LMFP/C-F/G at a rate of 0.1C. After 50 cycles of charge and discharge, the capacity retention rate is more than 95.3%. After 100 cycles, the capacity retention rate remains above 85.8%. These results indicates that the material exhibits good cyclic performance in the coin battery. Furthermore, even after hundreds of cycles, the Coulomb efficiency remained at about 99.5%.

To further compare the charge-discharge performance and rate performance of three samples, we summarized them in Figure 7a,b. It can be seen that the discharge performance and rate performance of LMFP/C-F/G samples are significantly better than those of the other two materials. The remarkable performance of LMFP/C-F/G cathode material can be attributed to various factors: (1) nano-crystallization and a well-defined, uniform morphology; (2) enhanced electronic conductivity achieved through a combination of mixed carbon sources and uniform coating; (3) establishment of a rapid ion/electron conduction network, characterized by a 'point-to-surface' architecture; and (4) improved electrochemical kinetics facilitated by regulation through anion doping.

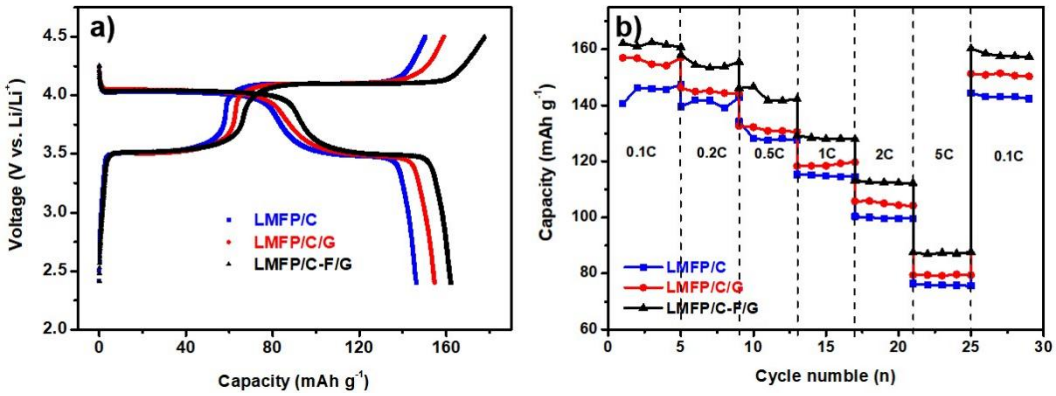

Figure 7. Electrochemical performance of three samples at 25 °C: a) First three charge/discharge profiles at 0.1 C; b) Rate performance at different C rates.

3. Conclusions

In summary, a novel composite LMFP nanorods coated by F-doped carbon and graphene, forming a 'point-to-surface' conduction electron/ion network (LMFP/C-F/G), was successfully synthesized via a facile solvothermal reaction followed by one-step calcination process. XRD and XPS characterization results demonstrate that the LMFP solid solution material has been successfully synthesized. In addition, HRTEM characterization confirms that F has been successfully doped into the material and the surface is uniformly coated by an amorphous carbon layer of about 4 nm, which greatly reduces the charge transfer resistance and decreases polarization. Its unique electronic structure endows the material with rapid lithium-ion diffusion and electron transport capabilities, resulting in excellent electrochemical performance in terms of specific capacity, rate capability and cycle life. It exhibits an impressive discharge capacity of 163.1 mAh g^{-1} at a current rate of 0.1 C, with a Coulomb efficiency of 99.5% over 100 cycles. Moreover, it achieves an energy density as high as 607.6 Wh kg^{-1}, which surpasses that of most similar materials including commercial lithium iron phosphate. These results further demonstrate that the electrochemical performance of lithium manganese phosphate can be effectively improved through a dual strategy of carbon coating and F-doping.

4. Patents

Application number: 202410340091.7

 doi:10.20944/preprints202405.1101.v1

Supplementary Materials: The following supporting information can be downloaded at the website of this paper posted on Preprints.org, Experimental section; Figure S1: a-b) SEM image of the LMFP/C-F/G nanorods and c-d) graphene, Figure S2: a) XPS survey spectra of LFMP/C and the high-resolution spectrum of b) Fe 2p; c) Mn 2p; d) C 1s; e) O 1s; f) P 2p; g) Li 1s, Figure S3: a) XPS survey spectra of LFMP/C/G and the high-resolution spectrum of b) Fe 2p; c) Mn 2p; d) C 1s; e) O 1s; f) P 2p; g) Li 1s, Figure S4: Electrochemical performance of LMFP/C/G at 25 °C: a) First three charge/discharge profiles at 0.1 C; b) Rate performance at different C rates and c) Corresponding charge/discharge curves, Figure S5: Electrochemical performance of LMFP/C at 25 °C: a) First three charge/discharge profiles at 0.1 C; b) Rate performance at different C rates and c) Corresponding charge/discharge curves, Table S1: The discharge capacity at different C rates and corresponding energy density of the three materials were studied, Table S2: The lithium ion diffusion coefficient D_{Li+} of the cathode materials were calculated from the Randles-Sevcik formula, Table S3: Comparison of properties of LMFP materials.

Author Contributions: Conceptualization, H.W., M.T., Q.L. and B.L.; methodology and writing—original draft preparation, H.W., M.T., Q.L. and B.L.; writing—review and editing, H.W., M.T., Q.L., Z.Y. and B.L.; supervision, M.T. and B.L. All authors have read and agreed to the published version of the manuscript.

Data Availability Statement: Data sharing is not applicable to this article.

Acknowledgments: We would like to thank Editage (www.editage.cn) for English language editing.

Conflicts of Interest: The authors declare no conflict of interest.

References

1. Armand, M.; Tarascon, J. M., Building better batteries. *Nature* **2008,** 451, 652-657.
2. Li, F.; He, J.; Liu, J.; Wu, M.; Hou, Y.; Wang, H.; Qi, S.; Liu, Q.; Hu, J.; Ma, J., Gradient Solid Electrolyte Interphase and Lithium-Ion Solvation Regulated by Bisfluoroacetamide for Stable Lithium Metal Batteries. *Angewandte Chemie International Edition* **2021,** 60, 6600-6608.
3. Di Lecce, D.; Hassoun, J., Lithium Transport Properties in $LiMn_{1-\alpha}Fe_{\alpha}PO_4$ Olivine Cathodes. *The Journal of Physical Chemistry C* **2015,** 119, 20855-20863.
4. A. K. Padhi, K. S. N., J. B. Goodenough, Phospho-olivines as Positive-Electrode Materials for Rechargeable Lithium Batteries. *Journal of The Electrochemical Society* **1997,** 144, 1188.
5. Guo, H.; Liu, R.; Li, W.; Gu, H.; Cao, J.; Gong, D.; Liang, G., Site Selection of Niobium-Doped $LiMn_{0.6}Fe_{0.4}PO_4$ and Effect on Electrochemical Properties. *Journal of The Electrochemical Society* **2023,** 170, 030542.
6. Gao, C.; Zhou, J.; Liu, G.; Wang, L., Synthesis of F-doped $LiFePO_4$/C Cathode Materials for High Performance Lithium-ion Batteries using Co-Precipitation Method with Hydrofluoric Acid Source. *Journal of Alloys and Compounds* **2017,** 727, 501-513.
7. Gangaraju, V.; Shastri, M.; Shetty, K.; Marilingaiah, N. R.; Anantharaju, K. S.; Shivaramu, P. D.; Rangappa, D., In-situ Preparation of Silk-Cocoon Derived Carbon and $LiFePO_4$ Nanocomposite as Cathode Material for Li-ion Battery. *Ceramics International* **2022,** 48, 35657-35665.
8. Liu, Y.; Gu, J.; Zhang, J.; Wang, J.; Nie, N.; Fu, Y.; Li, W.; Yu, F., Controllable Synthesis of Nano-Sized $LiFePO_4$/C via a High Shear Mixer Facilitated Hydrothermal Method for High Rate Li-ion Batteries. *Electrochimica Acta* **2015,** 173, 448-457.
9. Zhang, W. J., Structure and Performance of $LiFePO_4$ Cathode Materials: A Review. *Journal of Power Sources* **2011,** 196, 2962-2970.
10. Jiang, F.; Qu, K.; Wang, M. S.; Chen, J. C.; Liu, Y.; Xu, H.; Huang, Y.; Li, J. Y.; Gao, P.; Zheng, J. M.; Chen, M. Y.; Li, X., Atomic Scale Insight into the Fundamental Mechanism of Mn Doped $LiFePO_4$. *Sustainable Energy & Fuels* **2020,** 4, 2741-2751.
11. Luo, T.; Zeng, T. T.; Chen, S. L.; Li, R.; Fan, R. Z.; Chen, H.; Han, S. C.; Fan, C. L., Structure, Performance, Morphology and Component Transformation Mechanism of $LiMn_{0.8}Fe_{0.2}PO_4$/C Nanocrystal with Excellent Stability. *Journal of Alloys and Compounds* **2020,** 834, 155143.
12. Oh, S. M.; Myung, S. T.; Park, J. B.; Scrosati, B.; Amine, K.; Sun, Y. K., Double-Structured $LiMn_{0.85}Fe_{0.15}PO_4$ Coordinated with $LiFePO_4$ for Rechargeable Lithium Batteries. *Angewandte Chemie International Edition* **2012,** 51, 1853-1856.
13. Yang, J.; Tan, R.; Li, D.; Ma, J. M.; Duan, X. C., Ionic Liquid Assisted Electrospinning of Porous $LiFe_{0.4}Mn_{0.6}PO_4$/CNFs as Free-Standing Cathodes with a Pseudocapacitive Contribution for High-Performance Lithium-Ion Batteries. *Chemistry – A European Journal* **2020,** 26, 5341-5346.
14. Deng, Y.; Yang, C.; Zou, K.; Qin, X.; Zhao, Z.; Chen, G., Recent Advances of Mn-Rich $LiFe_{1-y}Mn_yPO_4$ ($0.5 \leq y < 1.0$) Cathode Materials for High Energy Density Lithium Ion Batteries. *Advanced Energy Materials* **2017,** 7, 1601958.
15. Xiong, J. W.; Wang, Y. Z.; Wang, Y. Y.; Zhang, J. X., PVP-Assisted Solvothermal Synthesis of $LiMn_{0.8}Fe_{0.2}PO_4$/C Nanorods as Cathode Material for Lithium Ion Batteries. *Ceramics International* **2016,** 42, 9018-9024.

 doi:10.20944/preprints202405.1101.v1

16. Peng, Z. D.; Zhang, B. C.; Hu, G. R.; Du, K.; Xie, X. M.; Wu, K. P.; Wu, J. H.; Gong, Y. F.; Shu, Y. M.; Cao, Y. B., Green and Efficient Synthesis of Micro-Nano $LiMn_{0.8}Fe_{0.2}PO_4$/C Composite with High-Rate Performance for Li-ion Battery. *Electrochimica Acta* **2021,** 387, 138456.
17. Yang, S. C.; Zhou, C. C.; Wang, Q.; Chen, B. B.; Zhao, Y.; Guo, B.; Zhang, Z. J.; Gao, X. L.; Chowdhury, R.; Wang, H. Z.; Lai, C.; Brandon, N. P.; Wu, B.; Liu, X. H., Highly Aligned Ultra-Thick Gel-Based Cathodes Unlocking Ultra-High Energy Density Batteries. *Energy & Environmental Materials* **2022,** 5, 1332-1339.
18. Wang, Y.; Niu, P.; Li, J. Z.; Wang, S. L.; Li, L., Recent Progress of Phosphorus Composite Anodes for Sodium/Potassium Ion Batteries. *Energy Storage Materials* **2021,** 34, 436-460.
19. Hu, H.; Li, H.; Lei, Y.; Liu, J.; Liu, X.; Wang, R.; Peng, J.; Wang, X., Mg-doped $LiMn_{0.8}Fe_{0.2}PO_4$/C Nano-Plate as a High-Performance Cathode Material for Lithium-ion Batteries. *Journal of Energy Storage* **2023,** 73, 109006.
20. Wu, R.; Drozdov, I. K.; Eltinge, S.; Zahl, P.; Ismail-Beigi, S.; Bozovic, I.; Gozar, A., Large-Area Single-Crystal Sheets of Borophene on Cu(111) Surfaces. *Nature Nanotechnology* **2019,** 14, 44-49.
21. Karimzadeh, S.; Safaei, B.; Huang, W.; Jen, T. C., Theoretical Investigation on Niobium Doped $LiFePO_4$ Cathode Material for High Performance Lithium-ion Batteries. *Journal of Energy Storage* **2023,** 67, 107572.
22. Sahoo, P. K.; Memaran, S.; Xin, Y.; Balicas, L.; Gutierrez, H. R., One-pot growth of two-dimensional lateral heterostructures via sequential edge-epitaxy. *Nature* **2018,** 553, 63-67.
23. Yang, L.; Deng, W.; Xu, W.; Tian, Y.; Wang, A.; Wang, B.; Zou, G.; Hou, H.; Deng, W.; Ji, X., Olivine $LiMn_xFe_{1-x}PO_4$ Cathode Materials for Lithium Ion Batteries: Restricted Factors of Rate Performances. *Journal of Materials Chemistry A* **2021,** 9, 14214-14232.
24. Luo, C.; Jiang, Y.; Zhang, X. X.; Ouyang, C. Y.; Niu, X. B.; Wang, L. P., Misfit Strains Inducing Voltage Decay in $LiMnyFe_{1-y}PO_4$/C. *Journal of Energy Chemistry* **2022,** 68, 206-212.
25. Song, Y.; Liu, Y.; Ou, X., Heat-Rate-Controlled Hydrothermal Crystallization of High-Performance $LiMn_{0.7}Fe_{0.3}PO_4$ Cathode Material for Lithium-ion Batteries. *Ceramics International* **2020,** 46, 5069-5076.
26. Hidalgo, J.; An, Y.; Yehorova, D.; Li, R.; Breternitz, J.; Perini, C. A. R.; Hoell, A.; Boix, P. P.; Schorr, S.; Kretchmer, J. S.; Correa-Baena, J.-P., Solvent and A-Site Cation Control Preferred Crystallographic Orientation in Bromine-Based Perovskite Thin Films. *Chemistry of Materials* **2023,** 35, 4181-4191.
27. Yan, X.; Sun, D.; Wang, Y.; Zhang, Z.; Yan, W.; Jiang, J.; Ma, F.; Liu, J.; Jin, Y.; Kanamura, K., Enhanced Electrochemical Performance of $LiMn_{0.75}Fe_{0.25}PO_4$ Nanoplates from Multiple Interface Modification by Using Fluorine-Doped Carbon Coating. *ACS Sustainable Chemistry & Engineering* **2017,** 5, 4637-4644.
28. Ming, L.; Zhang, B.; Cao, Y.; Zhang, J. F.; Wang, C. H.; Wang, X. W.; Li, H., Effect of Nb and F Co-doping on $Li_{1.2}Mn_{0.54}Ni_{0.13}Co_{0.13}O_2$ Cathode Material for High-Performance Lithium-Ion Batteries. *Frontiers in Chemistry* **2018,** 6, 76.
29. Wang, X.; Feng, Z.; Huang, J.; Deng, W.; Li, X.; Zhang, H.; Wen, Z., Graphene-Decorated Carbon-Coated $LiFePO_4$ Nanospheres as a High-Performance Cathode Material for Lithium-Ion Batteries. *Carbon* **2018,** 127, 149-157.
30. Ding, D.; Maeyoshi, Y.; Kubota, M.; Wakasugi, J.; Kanamura, K.; Abe, H., Highly Improved Performances of $LiMn_{0.7}Fe_{0.3}PO_4$ Cathode with in Situ Electrochemically Reduced Graphene Oxide. *Journal of Alloys and Compounds* **2019,** 793, 627-634.
31. Ding, D.; Maeyoshi, Y.; Kubota, M.; Wakasugi, J.; Kanamura, K.; Abe, H., Holey Reduced Graphene Oxide/Carbon Nanotube/$LiMn_{0.7}Fe_{0.3}PO_4$ Composite Cathode for High-Performance Lithium Batteries. *Journal of Power Sources* **2020,** 449, 227553.
32. Ma, F.; Zhang, X.; He, P.; Zhang, X.; Wang, P.; Zhou, H., Synthesis of Hierarchical and Bridging Carbon-Coated $LiMn_{0.9}Fe_{0.1}PO_4$ Nanostructure as Cathode Material with Improved Performance for Lithium Ion Battery. *Journal of Power Sources* **2017,** 359, 408-414.
33. Wang, B.; Liu, A.; Abdulla, W. A.; Wang, D.; Zhao, X. S., Desired Crystal oriented $LiFePO_4$ Nanoplatelets in Situ Anchored on a Graphene Cross-Linked Conductive Network for Fast Lithium Storage. *Nanoscale* **2015,** 7, 8819-8828.
34. Wei, H. L.; Tan, A. D.; Hu, S. Z.; Piao, J. H.; Fu, Z. Y., Efficient Spinel Iron-Cobalt Oxide/Nitrogen-Doped Ordered Mesoporous Carbon Catalyst for Rechargeable Zinc-Air Batteries. *Chinese Journal of Catalysis* **2021,** 42, 1451-1458.
35. Lv, X. Y.; Huang, Q. Y.; Wu, Z.; Su, J.; Long, Y. F.; Wen, Y. X., $Li_{0.995}Nb_{0.005}Mn_{0.85}Fe_{0.15}PO_4$/C as a High-Performance Cathode Material for Lithium-Ion Batteries. *Journal of Solid State Electrochemistry* **2017,** 21, 1499-1507.
36. Zhang, K.; Lee, J. T.; Li, P.; Kang, B.; Kim, J. H.; Yi, G.-R.; Park, J. H., Conformal Coating Strategy Comprising N-doped Carbon and Conventional Graphene for Achieving Ultrahigh Power and Cyclability of $LiFePO_4$. *Nano Letters* **2015,** 15, 6756-6763.
37. Xiao, P.; Cai, Y. Y.; Chen, X. P.; Sheng, Z. M.; Chang, C. K., Improved Electrochemical Performance of $LiFe_{0.4}Mn_{0.6}PO_4$/C with Cr^{3+} Doping. *RSC Advances* **2017,** 7, 31558-31566.

 doi:10.20944/preprints202405.1101.v1

38. Liu, Z.; Wang, K.; Li, Y.; Yuan, S.; Huang, G.; Li, X.; Li, N., Activation Engineering on Metallic 1T-MoS_2 by Constructing In-Plane Heterostructure for Efficient Hydrogen Generation. *Applied Catalysis B: Environmental* **2022,** 300, 120696.
39. Ding, D.; Maeyoshi, Y.; Kubota, M.; Wakasugi, J.; Kanamura, K.; Abe, H., A Facile Way To Synthesize Carbon-Coated $LiMn_{0.7}Fe_{0.3}PO_4$/Reduced Graphene Oxide Sandwich-Structured Composite for Lithium-Ion Batteries. *ACS Applied Energy Materials* **2019,** 2, 1727-1733.
40. Huang, Y.; Ding, R.; Ying, D.; Shi, W.; Huang, Y.; Tan, C.; Sun, X.; Gao, P.; Liu, E., Engineering doping-vacancy double defects and insights into the conversion mechanisms of an Mn–O–F ultrafine nanowire anode for enhanced Li/Na-ion storage and hybrid capacitors. *Nanoscale Advances* **2019,** 1, 4669-4678.
41. Qin, Q.; Deng, N.; Wang, L.; Zhang, L.; Jia, Y.; Dai, Z.; Liu, Y.; Kang, W.; Cheng, B., Novel Flexible Mn-Based Carbon Nanofiber Films as Interlayers for Stable Lithium-Metal Battery. *Chemical Engineering Journal* **2019,** 360, 900-911.
42. Zhang, K.; Cao, J.; Tian, S.; Guo, H.; Liu, R.; Ren, X.; Wen, L.; Liang, G., The Prepared and Electrochemical Property of Mg-Doped $LiMn_{0.6}Fe_{0.4}PO_4$/C as Cathode Materials for Lithium-Ion Batteries. *Ionics* **2021,** 27, 4629-4637.
43. Kou, L. Q.; Chen, F. J.; Tao, F.; Dong, Y.; Chen, L., High Rate Capability and Cycle Performance of Ce-Doped $LiMnPO_4$/C via an Efficient Solvothermal Synthesis in Water/Diethylene Glycol System. *Electrochimica Acta* **2015,** 173, 721-727.
44. Li, N.; Xu, Z.; Wang, P.; Zhang, Z.; Hong, B.; Li, J.; Lai, Y., High-Rate Lithium-Sulfur Batteries Enabled via Vanadium Nitride Nanoparticle/3D Porous Graphene through Regulating the Polysulfides Transformation. *Chemical Engineering Journal* **2020,** 398, 125432.
45. Sun, Z. H.; Wu, X. L.; Peng, Z. Q.; Wang, J. W.; Gan, S.; Zhang, Y. W.; Han, D. X.; Niu, L., Compactly Coupled Nitrogen-Doped Carbon Nanosheets/Molybdenum Phosphide Nanocrystal Hollow Nanospheres as Polysulfide Reservoirs for High-Performance Lithium–Sulfur Chemistry. *Small* **2019,** 15, 1902491.